Turkish Journal of Electrical Engineering & Computer Sciences

http://journals.tubitak.gov.tr/elektrik/

Research Article

Turk J Elec Eng & Comp Sci
(2014) 22: 1255 – 1269

doi:10.3906/elk-1210-93

pRediCS: A new GO-PO–based ray launching simulator for the calculation of electromagnetic scattering and RCS from electrically large and complex structures

Caner ÖZDEMİR*, Betül YILMAZ, Özkan KIRIK
Department of Electrical-Electronics Engineering, Mersin University, Yenişehir, Mersin, Turkey

Received: 22.10.2012 • **Accepted:** 13.02.2013 • **Published Online:** 15.08.2014 • **Printed:** 12.09.2014

Abstract: In this paper, we present a new simulator called pRediCS for the calculation of electromagnetic scattering and radar cross-section (RCS) from electrically large and complex targets. The simulator utilizes the geometric optics (GO) theory and launching of electromagnetic rays for tracing and calculating the electric field values as the electromagnetic waves bounce around the target. The physical optics (PO) theory is also exploited to calculate the final scattered electric field by calculating the far-field PO integration along the observation direction. The simulator is first tested with known objects of canonical shapes, whose analytical solutions are available in the literature. Next, our implemented GO-PO–type algorithm is validated by simulating the benchmark targets that have been well studied and documented by various studies. Finally, the RCS computation from complex and electrically large objects is calculated. By utilizing the RCS values for different frequencies and aspects, a successful inverse synthetic aperture radar image of the target with fast simulation time is achieved.

Key words: Electromagnetic scattering, inverse synthetic aperture radar, numerical electromagnetics, radar cross-section, shooting and bouncing rays

1. Introduction

The calculation of radar cross-section (RCS) from electrically large and complex-shaped objects has been a great research topic for decades [1–4]. The RCS information of a military platform is very crucial, especially for electronic warfare applications. Radar detection and guided missile tracking can only be possible for sufficiently large RCS values. Therefore, the need for simulating the RCS of military platforms is essential since it is much cheaper, practical, faster, and more reliable than constructing a RCS measurement setup or a real scenario. With the aid of such simulators [5–9], it becomes possible to tweak and design various parameters that affect the RCS of a target. These studies include low-observability or RCS reduction studies [10], inverse synthetic aperture radar (ISAR) imaging applications [11], and constructing radar signature databases [12].

Many methods, from full-wave solutions to asymptotic or hybrid techniques, have been employed for the calculation of electrically large and complex platforms. Full-wave solutions like the method of moments (MoM), finite difference time domain method, and finite element method provide robust calculation of the RCS of such structures whose sizes are at most a few wavelengths for nominal computers [5–8]. Although these methods can handle over a billion unknowns [9], powerful computer hardware is still needed to be able to calculate the RCS values of large and complex bodies. Therefore, the computational load based on the memory and

*Correspondence: cozdemir@mersin.edu.tr

simulation time required for the RCS calculation of electrically large and complex objects is not manageable, even for today's powerful computers. This is because full-wave methods usually deal with an unknown matrix of impedances or equivalent parameters. At high frequencies, of course, the size of this matrix becomes very huge. For that reason, the computation memory requirement to store this matrix and the computation time to invert it grow to be gigantic for electrically large and complex bodies. On the other hand, asymptotic or hybrid techniques based on geometric optics (GO) or physical optics (PO) solutions have been much more efficiently applied for the RCS simulation of such structures [13]. The shooting and bouncing ray (SBR), a hybrid method that combines GO with PO, has been the pioneering technique for fast and efficient calculation of RCS from such targets at high frequencies [14,15]. The SBR method is based on the launching of a dense set of optical rays and tracing these rays according to the GO and PO theory [14]. With this construct, it is conceptually very different and also computationally much more efficient than full-wave methods. Aside from these benefits, only a limited number of researchers put effort into studying and enhancing SBR-based algorithms [16,17] since its first introduction to the electromagnetic (EM) community by Ling et al. [14,15]. Jin et al. provided a hybrid technique that combines the SBR with MoM for analyzing RCS from large conducting bodies with small protrusions [16]. Chen and Jeng utilized the SBR for the investigation of indoor radio-wave propagation [18]. Recently, Weinmann developed a new simulator for the implementation of the SBR technique [19], and, more recently, Tao et al. implemented the SBR for faster RCS calculation by utilizing graphics processing units (GPUs) [17].

Since studies dedicated to the SBR and other hybrid or asymptotic methods have been limited, there are only a few simulators developed and available in the literature [20–23]. Furthermore, some of these simulators are not publicly or commercially accessible and some of them have limitations for different and special scenarios. For these reasons, we set out to develop a new and fast simulator for the implementation of the SBR theory that combines the GO theory with the PO theory, such that EM scattering and the RCS from electrically large and complex-shaped structures can be successfully and efficiently predicted. In the next section, we present the algorithm behind our implementation of the SBR technique. In Section 3, our RCS simulator code, called pRediCS, is introduced and tested with various benchmark targets whose RCS values can be readily obtained from the literature. Furthermore, the simulator is also used to find the EM scattering of a large and complex platform. The resultant RCS, range profile, and ISAR image for the selected platform are also constructed. We also simulate these objects with the commercially available EM structure simulator code FEKO [24] so that we can compare our results with a reliable simulator in terms of accuracy and computation time. In the last section, computation time values for the simulated structures are given. It is shown that our simulator is highly efficient while simulating large and complex bodies. The work is concluded by referring to future improvements for the simulator.

2. Scattered field calculation using the GO-PO theory

Our implementation of the RCS calculation is based on the employment of ray launching with the GO theory and the application of the PO theory afterwards.

2.1. Launching rays and tracing the field via GO

We begin the implementation of our simulator by assuming that both the transmitter and the receiver are located at the far field of the target. Therefore, the incident electric field can be assumed to be in the form of

a plane wave, as given below:

$$\vec{E}^{inc}(r) = \vec{E} \cdot \exp(-j\vec{k}^i \cdot \vec{r}), \tag{1}$$

where $\vec{E} = E_\theta \cdot \hat{\theta}^i + E_\emptyset \cdot \hat{\emptyset}^i$ corresponds to vertically and horizontally polarized components of the incoming wave and $\vec{k}^i$ is the incident wave-number vector given by:

$$\vec{k}^i = k \sin\theta^i \cos\emptyset^i \cdot \hat{x} + k \sin\theta^i \sin\emptyset^i \cdot \hat{y} + k \cos\theta^i \cdot \hat{z}, \tag{2}$$

where $k = 2\pi f/c$ is the wave number corresponding to the frequency variable f. The incident electric field, assumed to be discretized by a dense set of rays, is launched from a hypothetical transmitter at the far-field towards the object along the direction of $\vec{k}^i$. Based on the far-field assumption, all of the rays that hit the target are parallel to each other as illustrated in Figure 1. For a reliable solution, the ray density should be selected as at least 10 rays per wavelength as the common practice [19].

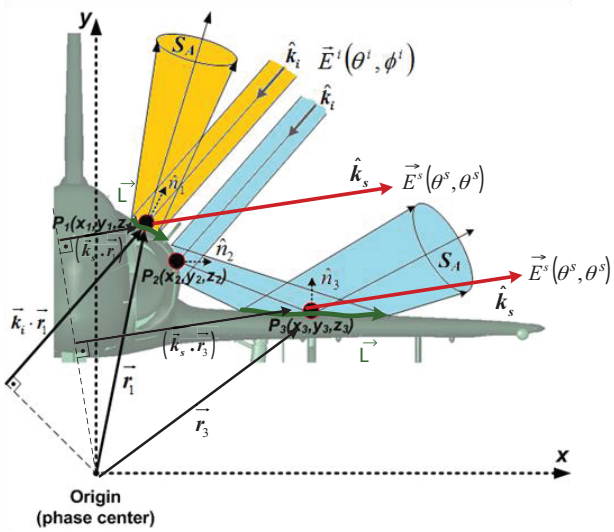

Figure 1. Geometry for the ray tracing and GO theory. The PO theory is applied to find the scattered field along the observation direction.

In our simulator, we assume that the origin is the phase center of the scene. As demonstrated in Figure 1, the incident electric field that hits a point (say $P_1(x_1y_1z_1)$) on the object has the following form:

$$\vec{E}^{inc}\Big|_{@r_1} = \vec{E} \cdot \exp(j\vec{k}^i \cdot \vec{r}_1). \tag{3}$$

When the rays hit the target, they start to bounce around it. The rays are traced with the rules of the GO theory while bouncing around the object. As the optical ray tracing has to be carefully employed based on the Snell law of reflection, the amplitude and phase of the electric field need to be traced as well. While some rays may experience only a single bounce, some others may have multiple bounces (see Figure 1). For the mth ray, let us assume a total of N bounce mechanisms before it leaves the object. Therefore, the mth ray hits $P_n^m(x_n y_n z_n)$ points on the surface of the target ($n = 1, 2, .., N$). At this point, we apply the amplitude tracking methodology that was first introduced and applied in [14]. Therefore, the electric-field value around the nth

hit point $P_n^m(x_n y_n z_n)$ can be found via:

$$\vec{E}_{n-1}^m(x_n y_n z_n) = (DF)_{n-1}^m \cdot (\Gamma)_{n-1}^m \cdot \vec{E}_{n-1}^m(x_{n-1} y_{n-1} z_{n-1}) \cdot \exp(-jk \cdot R_{(n-1)\to n}^m), \tag{4}$$

where $\vec{E}_{n-1}^m(x_{n-1} y_{n-1} z_{n-1})$ is the electric field value at the $(n-1)$th hit point and $P_{n-1}^m(x_{n-1} y_{n-1} z_{n-1})$ for the mth ray. Here, $(DF)_{n-1}^m$ corresponds to the ray tube divergence factor for the $(n-1)$th hit of the mth ray. As illustrated in Figure 1, (DF) spreads while rays are bouncing around the target. For targets that have planar surfaces, the divergence factor is 1 as the rays keep their parallel alignment with respect to each other after bouncing from the surface. For targets that have curved surfaces, the spreading of the rays causes the amplitude of the ray fields to decrease. The detailed derivation of the ray divergence can be found in [10,11,14,15] and will not be repeated here.

In the above equation $(\Gamma)_{n-1}^m$ is the reflection coefficient at point P_{n-1} for the mth ray. For perfect electric conductors (PECs), the magnitude of the reflection coefficient is unity. For planar surfaces of the PEC, the reflected field for the nth hit can be calculated by:

$$\vec{E}_n^{ref} = -\vec{E}_n^i + 2\left(\hat{s} \times \vec{E}_n^i\right) \times \hat{s}, \tag{5}$$

where $\vec{E}_n^i$ is the incoming electric field before the nth bounce and $\hat{s}$ is the normal of the surface. When the PEC surface is coated with a dielectric or magnetic layer, the transmission line equivalent of the coating can be implemented such that reflection coefficients for the transverse electric and the transverse magnetic wave polarizations can be calculated as given in [14].

The phase term in Eq. (4) corresponds to the phase delay as the ray travels from point P_{n-1}^m to point P_n^m, in which $R_{(n-1)\to n}^m$ is the actual trip distance between these points:

$$R_{(n-1)\to n}^m = \left[(x_n - x_{n-1})^2 + (y_n - y_{n-1})^2 + (z_n - z_{n-1})^2\right]^{1/2}. \tag{6}$$

As demonstrated in Figure 1, the GO theory provides the reflected field from the surface according to the Snell law. This feature of GO may not be well suited for planar surfaces where the reflected field tends to scatter along the specular direction. For the far-field set-up, if the incoming wave is a plane wave, then the reflected wave is also a plane wave. This leads to a nonzero scattered field only along the specular direction, which is of course not correct. It is obvious that the scattered field from a planar surface such as a plate occurs in almost all directions but with different scattering amplitudes. Furthermore, the numerical calculation of the RCS from an object requires geometric (or computer-aided design, CAD) modeling of this object. The usual way of modeling an object is done with small patches of small planar surfaces. Therefore, the abovementioned feature of GO can be problematic when finding the scattered field from these small patches, as the reflected wave propagates only along the specular direction. To circumvent this problem, the PO theory comes into play, as we shall explain next.

2.2. Calculating the scattered field via PO

The scattered field calculation from the last bounce point, $P_n(x_n y_n z_n)$, is accomplished with the help of the PO approach [25], as demonstrated in Figure 1. According to the PO theory, the incoming electric field for

the mth ray, $\vec{E}_n^m$, produces an equivalent surface current density of $\vec{J}^m(S_A)$, which can be approximated as:

$$\vec{J}^m(S_A) \cong 2 \cdot \vec{E}_n^m(x_n y_n z_n) \times \hat{s}_N, \tag{7}$$

where $\hat{s}_N$ is the surface normal at the last hit point and S_A is the ray tube area. As the last step, the PO integration is carried out to find the far field scattered field contribution of the mth ray due to this surface current:

$$\vec{E}^m(k) = j\frac{k\eta}{4\pi r} \cdot \iint\limits_{S_A} \vec{J}^m(S_A) \cdot \exp\left(j\vec{k}^s \cdot \vec{r}_N^m\right) \cdot d\vec{S}. \tag{8}$$

Here, $\vec{k}^s$ is the wave number vector along the scattering direction and is given by:

$$\vec{k}^s = k\sin\theta^s\cos\emptyset^s \cdot \hat{x} + k\sin\theta^s\sin\emptyset^s \cdot \hat{y} + k\cos\theta^s \cdot \hat{z}, \tag{9}$$

and $\eta = (\mu/\epsilon)^{1/2}$ is the intrinsic impedance of the propagating medium and $\vec{r}_N^m$ is the vector from the origin to the last bounce point $P_n^m(x_n y_n z_n)$ for the mth ray, provided that the origin is selected as the phase center of the scene. Of course, the above result is only valid for a single ray and the electric field contribution from all of the rays should be summed up to calculate the total scattered electric field $\vec{E}^s(k)$ as:

$$\vec{E}^s(k) = \sum_{m=1}^{M} \vec{E}^m(k), \tag{10}$$

where M is the total number of rays that hit the object. After completing the summation in Eq. (10), the scattered field is calculated at the specified frequency and angle.

3. Introducing the pRediCS EM simulator

The above summarized theory of the SBR is implemented in the C programming language for the purpose of calculating the EM scattering from complex-shaped objects of large electrical sizes. The simulator requires the CAD file of the object, which should be composed of sufficiently small triangular patches. The user interface is developed using Visual C++ and OpenGL is used for previewing the CAD model. It can support multiple simulation projects. Each project file is stored with the associated simulation parameters. Project details are saved on the MySQL database. The postprocessing tab of the code provides the plots of several metrics, including the scattered field, RCS, range profile, and ISAR image of the target. Some pictures from the interface of the simulator can be seen from Figure 2. The CAD selection window is given in Figure 2a and one of the simulator parameter selection windows is shown in Figure 2b.

3.1. Validation with benchmark objects

To assess the accuracy of our implementation of the SBR algorithm, various canonical objects, whose RCS has been either analytically calculated or is numerically well documented in the literature [26,27], are chosen. Our simulator is tested with these benchmark objects for different look angles and frequencies.

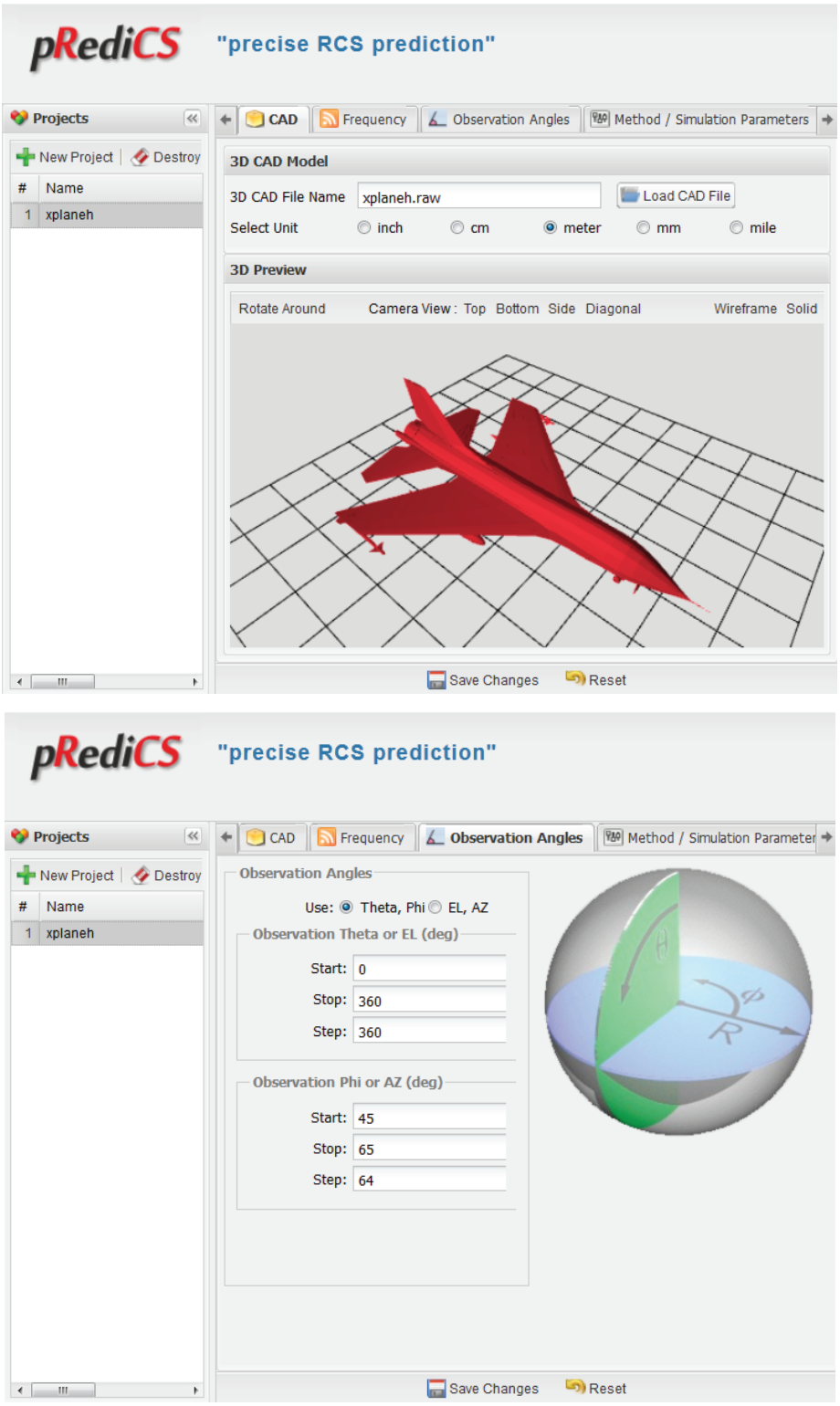

Figure 2. Some pictures from the interface of pRediCS: a) CAD file selection window and b) simulation parameter selection window.

3.1.1. Rectangular plate

As the first object, a perfectly conducting square plate is chosen, whose CAD file is given in Figure 3a. The monostatic RCS (or the backscattered RCS) simulation is carried out with the pRediCS code. For this simulation, the elevation angle variation of the simulator is tested such that EM backscattering from the object is calculated for different elevation angles that range from $\theta^i = \theta^s = 0^\circ$ to 180°, while the azimuth angle is set to $\emptyset^i = \emptyset^s = 0^\circ$, as illustrated in Figure 3a. The frequency of operation is taken as 10 GHz, such that the plate's electrical size becomes $12\,\lambda$ by $12\,\lambda$. The analytical solution for this geometry is available in [12] and plotted as the solid line in Figure 3b. Next, the backscattered electric field calculation of the geometry for the horizontal-horizontal (HH) polarization is done with our simulator. The resultant variations of the monostatic RCS for different elevation angles are calculated and plotted in Figure 3b as the dotted line. Finally, the monostatic RCS simulation of the object for HH polarization is carried out with FEKO and the result is drawn as the dashed line in Figure 3b for comparison. While our result almost perfectly coincides with the analytical solution, FEKO's simulation result matches well up to around –15 dBsm, as observed from Figure 3b.

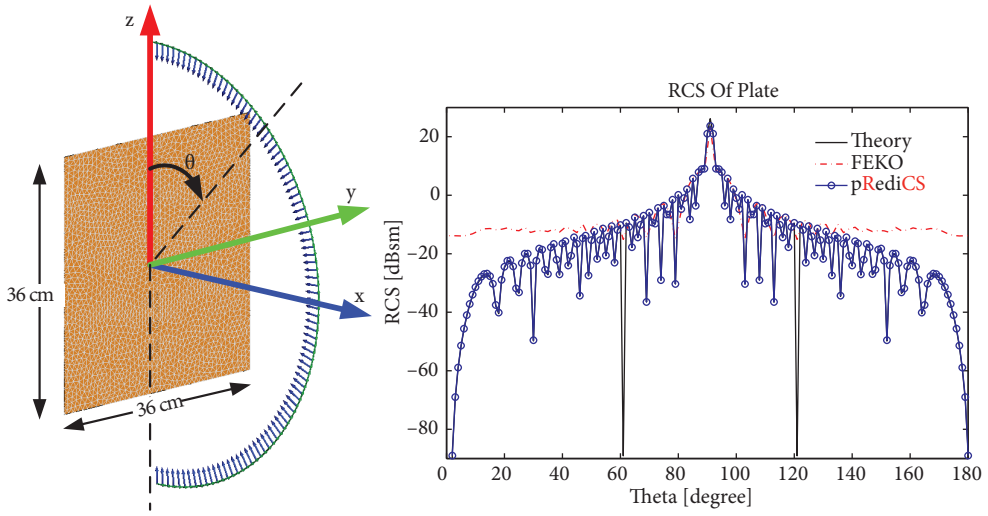

Figure 3. Monostatic RCS from the rectangular plate model: a) geometry for the simulation and b) RCS results for different elevation angles: analytical (solid), FEKO (dashed), and pRediCS (dotted).

3.1.2. Dihedral corner reflector

In the previous numerical example, the object provides only single-bounce mechanisms for the calculation of the RCS. Next, we test the accuracy of our simulator for the multibounce mechanism as well. For this goal, the dihedral corner reflector, whose geometry is shown in Figure 4a, is chosen as the second test object. This time, the azimuth variation for the single elevation value at $\theta^i = \theta^s = 90^\circ$ is tested. To compare our result with the other simulators, square plates that have side lengths of $5.6\,\lambda$ by $5.6\,\lambda$ are used to constitute the dihedral, as defined in [28]. Therefore, the side length of the plates is set to 17.90 cm for the chosen frequency of 9.4 GHz. The monostatic RCS for the vertical-vertical (VV) polarization that Griesser [28] found is plotted as the solid line in Figure 4b. The FEKO solution of the geometry is also presented in Figure 4b as the dashed line. The VV-polarized monostatic RCS that we calculated after running pRediCS is also drawn in Figure 4b as the dotted line, and, as is clearly seen, the result that we get with pRediCS fairly well matches Griessier's result and the FEKO solution.

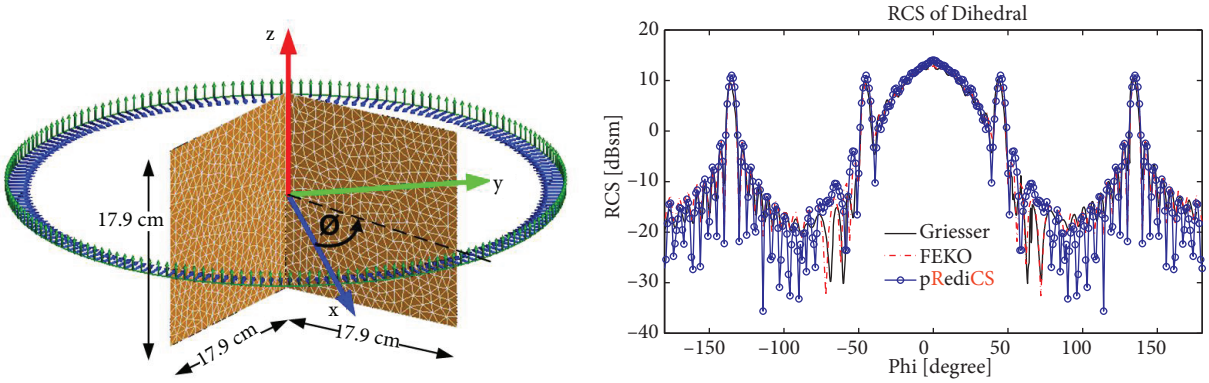

Figure 4. Backscattered RCS from the dihedral corner reflector model: a) geometry for the simulation and b) RCS results for different azimuth angles: Griesser's result (solid), FEKO (dashed), and pRediCS (dotted).

3.1.3. Triangular trihedral corner reflector

In this example, pRediCS is tested for frequency variation of the incoming wave. The triangular trihedral corner reflector, whose geometry given in Figure 5a, is chosen as the geometry to be simulated. This geometry provides the maximum value of the monostatic RCS when $\theta^i = \theta^s = 54.74^\circ$ and $\emptyset^i = \emptyset^s = 45^\circ$, as illustrated in Figure 5a. The analytical value for the monostatic RCS of the triangular trihedral corner reflector can be found in [29]. The monostatic RCS is plotted using the analytical formula in [29] for frequencies between 1 GHz and 9 GHz as the solid line in Figure 5b. Moreover, the FEKO simulation of this geometry for the VV polarization is also carried out for comparison purposes and drawn as the dashed line. The result that we obtain using pRediCS is shown as the dotted line that matches very well with the analytical solution. This clearly demonstrates the success of our simulator in predicting the EM scattering of multibounce mechanisms for different values of frequencies.

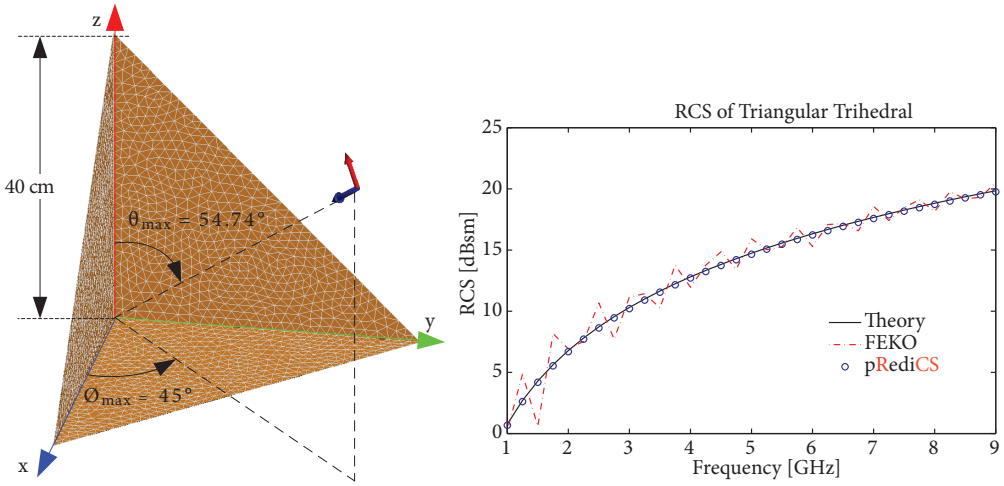

Figure 5. Backscattered RCS from the triangular trihedral corner reflector model: a) geometry for the simulation and b) RCS results for different frequencies: analytical (solid), FEKO (dashed), and pRediCS (dotted).

3.1.4. Cone-sphere

Cone-sphere geometry is one of the popular and most commonly used benchmark targets, whose RCS variation with respect to azimuth angles can be readily found in the literature [30,31]. The CAD file and simulation

geometry are shown in Figure 6a. The measured result of Griesser et al. [31] is plotted as the solid line in Figure 6b. The FEKO simulation is also carried out at 9 GHz for a total of 181181 discrete azimuth angles, ranging from $-180°$ to $0°0°$, and is drawn as the dashed line in Figure 6b. The CAD file of the cone-sphere is meshed in such a way that the maximum length of each triangular patch is equal to or less than one-tenth of the corresponding wavelength of 9 GHz. Our calculation of the RCS from the cone-sphere geometry with the same simulation parameters is given as the dotted line in Figure 6b. All of the results are provided for the HH polarization. Fair agreement of our simulation with the other references can also be easily observed from Figure 6b. Small differences between our results and the FEKO results are attributed to the different method (SBR vs. MoM) and meshing parameters of the CAD files that are used in different simulations. Moreover, small discrepancies between our results and the measured results can be explained by 2 main points: first, the measurements always include some shifts created by measurement errors, noises, and the imperfectness of the measurement setup. Second, pRediCS requires the discretization (i.e. meshing) of the curved surfaces of the cone-sphere structure. The approximate realization of curved structures with small planar patches is, of course, not perfect. Therefore, this can alter the RCS results within a small range, as expected.

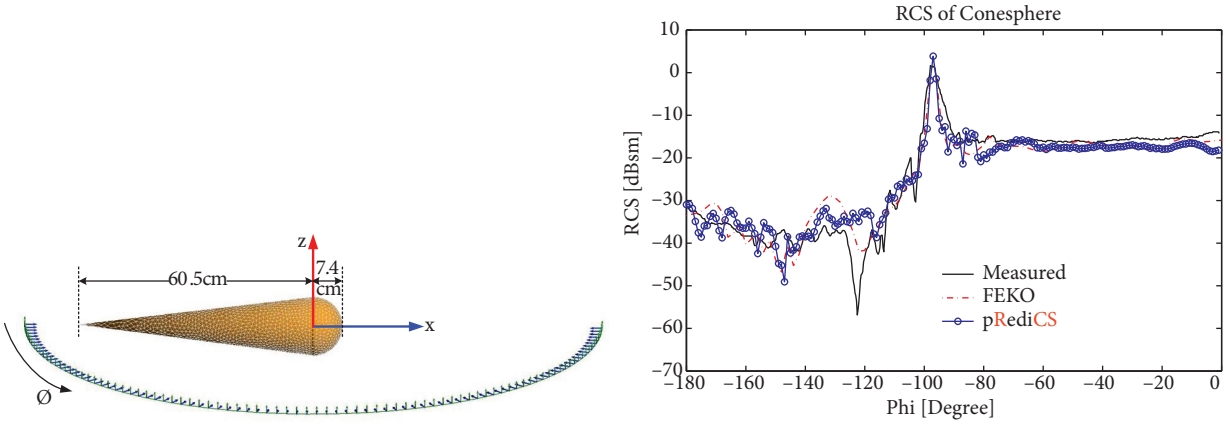

Figure 6. Monostatic RCS from the cone-sphere model: a) geometry for the simulation and b) RCS results for different azimuth angles: measurements taken from [31] (solid), FEKO (dashed), and pRediCS (dotted).

3.2. Simulation of a large and complex target

In the previous section, the validity and accuracy of our simulator is tested with canonical structures and benchmark targets. Now we can use the pRediCS code for the calculation of the EM scattering and RCS from an electrically large and complex target at high frequencies. The generic fighter called *xplaneh*, whose CAD file is shown in Figure 7a, is chosen. We carried out the EM backscattering simulation for the VV polarization from the model at the center frequency of 5 GHz. The backscattered electric field is collected for the nose-on case, within the frequency bandwidth of 500 MHz with 4.17 MHz frequency increments, such that a total of 120 discrete frequency points exist within the specified bandwidth. The RCS of the fighter is plotted in Figure 7b for the simulated frequencies. Next, we get the time domain backscattered response of the fighter by taking the inverse Fourier transform of these frequency-diverse data. Next, the range profile of the fighter can be readily constructed using the time-to-range transformation formula of $r = c \cdot t$. Here, c corresponds to the speed of light, and r and t are the range and time variables, respectively. The resultant range profile of the target from the nose-on case is given in Figure 7c, where the key hot points on the target can be easily deduced. As seen

from Figure 7c, the dominant scattering centers occur around the nose of the fighter. We also see significant backscattering energy from the wings, missiles, landing gear, and tails of the target.

Monostatic RCS of *xplaneh* over the azimuth angles is also calculated with our simulator to observe the RCS variation for different azimuth angles. While the monostatic elevation angle is set to 0°, the simulation is carried out at 9 GHz with 1° azimuthal angular increments. Next, the calculated monostatic RCS variation (in dBsm) over the azimuth angles is plotted in Figure 8.

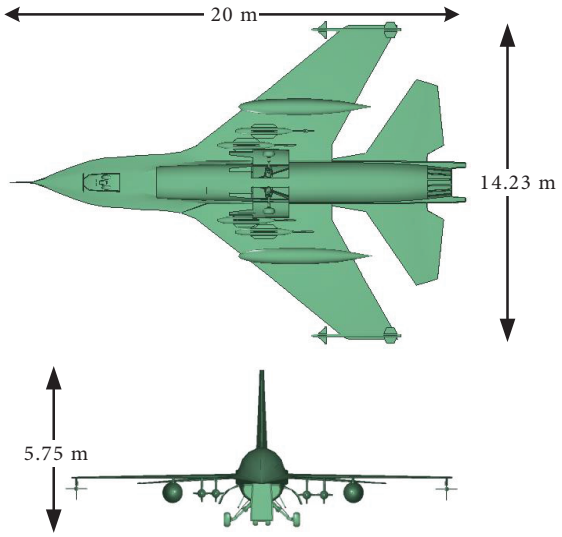

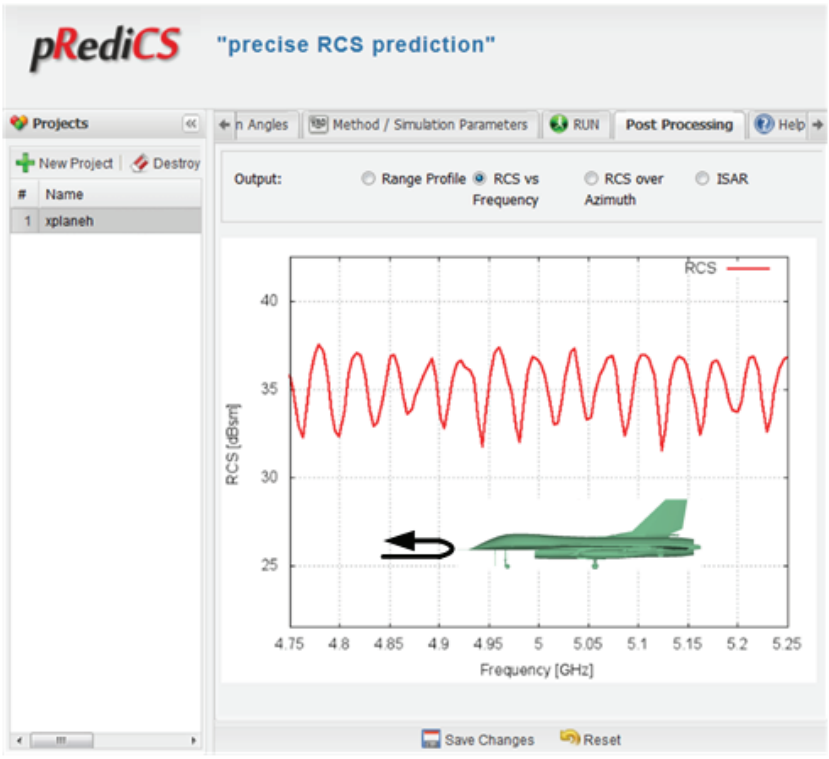

Figure 7. a) CAD file of a *xplaneh*, b) monostatic RCS for VV polarization from the nose-on case.

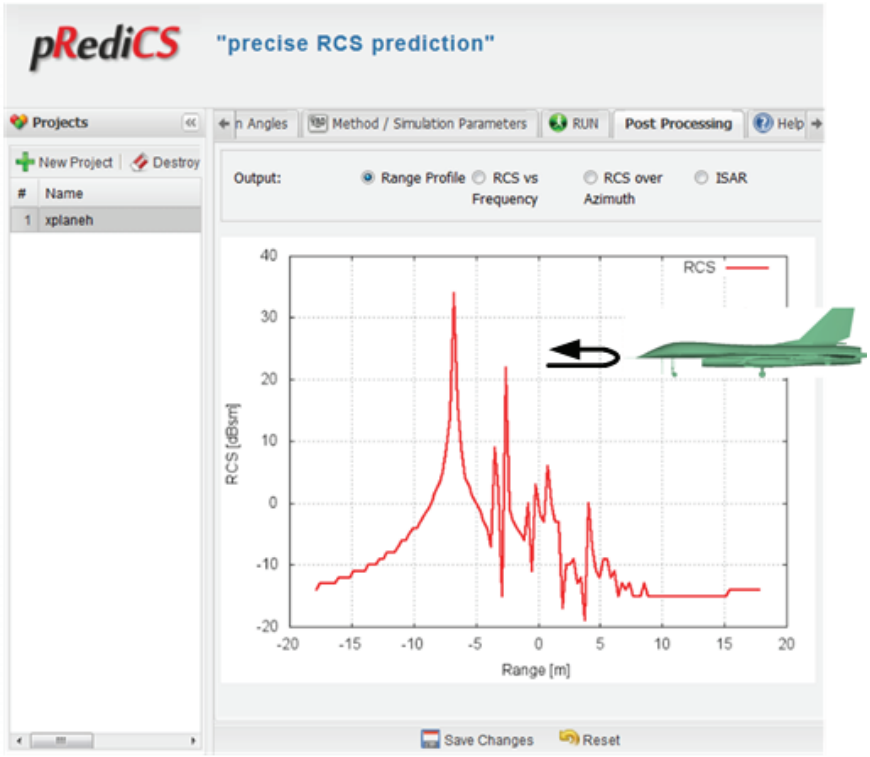

Figure 7. c) corresponding range profile.

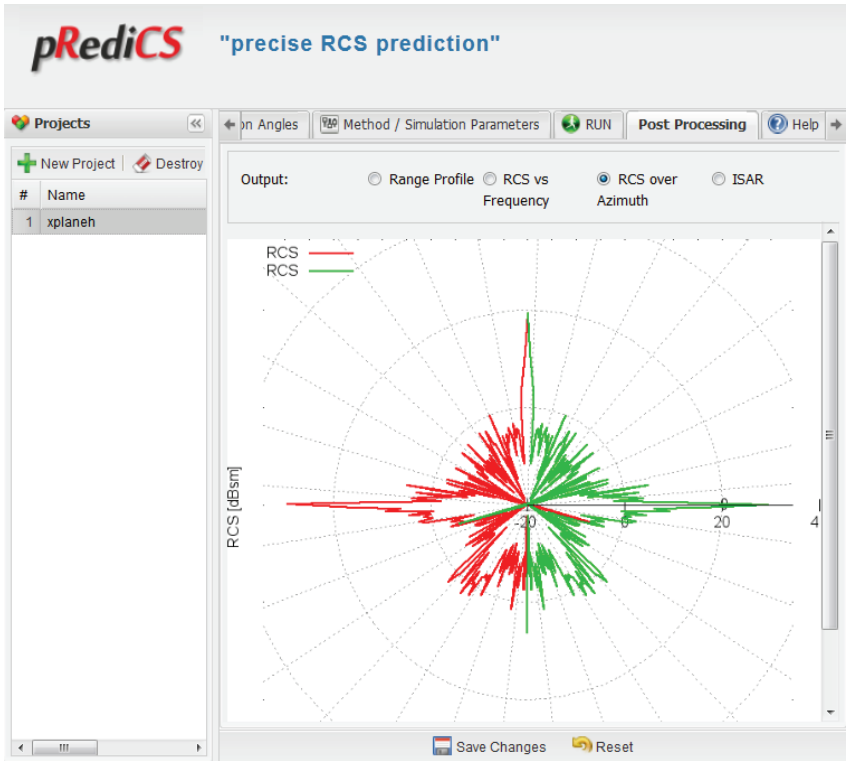

Figure 8. Monostatic RCS variation for the VV polarization (in dBsm) of *xplaneh* over the azimuth angles at 9 GHz.

Since pRediCS can calculate the RCS values from large and complex structures, we can also utilize it to construct the ISAR images of complex targets by calculating the EM scattering for multiple frequencies and multiple look angles. For this purpose, we compute the backscattered electric field for the VV polarization from xplaneh for the azimuth angles, ranging from 43.1° to 46.85°, for a total of 64 stepped frequencies. While the elevation look angle is kept at 60°, the frequency of the EM wave is altered between 5.9 GHz and 6.1 GHz, for a total of 32 distinct frequencies. Therefore, a total of 32 by 64 multifrequency multiaspect backscattered field data are collected with our simulation simulator. Using the conventional ISAR processing that was already given in [32] and [33], the ISAR image of *xplaneh* is gathered and shown in Figure 9, where it is seen that the scattering centers on the nose, landing gear, and missiles appear to be dominant for the selected look angle and the frequencies. As is obvious from Figure 9, pRediCS has the ability to calculate and plot the ISAR images of electrically large and complex targets.

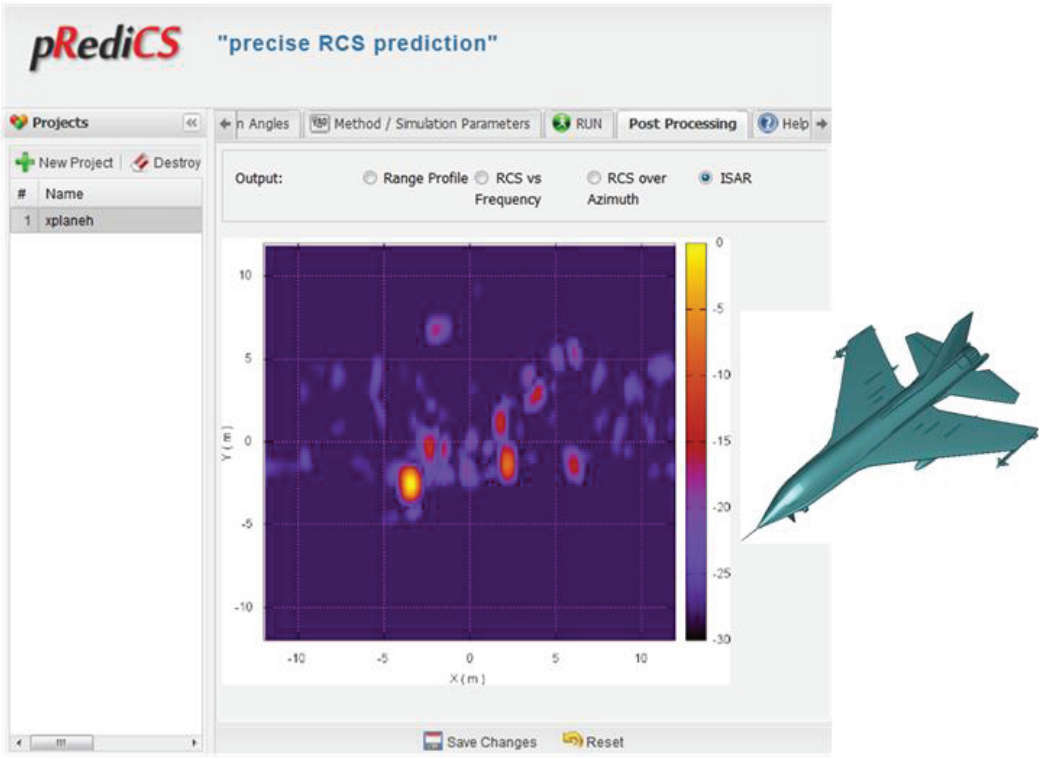

Figure 9. Monostatic ISAR image for the VV polarization of *xplaneh* at 45° from the nose-on.

4. Conclusion

In this work, we present a new simulator for the fast computation of EM scattering from electrically large and complex-shaped objects. The simulation of benchmark objects with our simulator demonstrated a very good match with the analytical/measured results from the literature. Therefore, the accuracy of our simulator for the RCS calculation was first validated with these reference results. Next, the prediction of RCS from a large and complex target was presented.

The Table lists the computation time values of the simulated structures using the FEKO simulator and those of pRediCS are provided for comparison. The simulations were run on a PC with a 1.73-GHz processor and 16 GB of RAM. As seen from the Table, our simulator can calculate simple structures such as plate,

dihedral, and trihedral on the order of only a few seconds. Although the simulation time for electrically large and complex targets increases, the total computation times are still on the order of minutes or hours, depending on the electrical size and complexity of the object.

Table. Computation time values for the simulated structures.

Target	Computation is done for.	Total computation time for single CPU	
		pRediCS	FEKO
Plate ($12\lambda \times 12\lambda$)	181 angles	8 s	380 s
Dihedral (each plate is $5.6\lambda \times 5.6\lambda$)	361 angles	10 s	109 s
Triangular trihedral (edge is 40 cm; frequencies from 1 *to* 9 GHz)	33 frequencies	4 s	782 h 55 min
Cone-sphere (length: $20.4\,\lambda$)	181 angles	9 min	108 h 20 min
(size: $\sim(316\lambda\,to\,350\lambda) \times(225\lambda\,to\,249\lambda)$)	120 frequencies	15 min	N/A
X planeh (size: $\sim 600\lambda \times 427\lambda$)	361 angles	38 h 50 min	N/A
(size: $\sim(393\lambda\,to\,406\lambda) \times(280\lambda\,to\,289\lambda)$)	32 frequencies $\times$64 angles	11 h 16 min	N/A

For the time being, the presented simulator can calculate only the scattering, not the diffracted field from PECs. In the near future, we plan to improve our simulator such that it may predict RCS from dielectric- or magnetic-coated structures as well. Furthermore, diffracted field contribution is also planned to be added to the total scattered field to have more accurate simulation of the scattered field, and we are planning to speed up the code by employing a message passing interface routine. Therefore, parallel processing of the code will be done in the near future, such that the code could be run on GPU-based machines for a much shorter simulation time.

References

[1] Youssef NN. Radar cross section of complex targets. Proc IEEE 1989; 77: 722–734.

[2] Rius JM, Ferrando M, Jofre L. High-frequency RCS of complex radar targets in real-time. IEEE T Antenn Propag 1993; 41: 1308–1319.

[3] Domingo M, Rivas F, Perez J, Torres RP, Catedra MF. Computation of the RCS of complex bodies modeled using NURBS surfaces. IEEE Antennas Propag 1995; 37: 36–47.

[4] Umashankar K, Taflove A. A novel method to analyze electromagnetic scattering of complex objects. IEEE T Electromagn C 1982; 24: 397–405.

[5] Luebbers R, Steich D, Kunz K. FDTD calculation of scattering from frequency-dependent materials. IEEE T Antenn Propag 1993; 41: 1249–1257.

[6] Sankar A, Tong TC. Current computation on complex structures by finite-element method. Electron Lett 1975; 11: 481–482.

[7] Ergül Ö, Malas T, Gürel L. Solutions of large-scale electromagnetics problems using an iterative inner-outer scheme with ordinary and approximate multilevel fast multipole algorithms. Progress in Electromagnetics Research 2010; 106: 203–223.

[8] Manyas A, Gürel L. Memory-efficient multilevel physical optics algorithm for fast computation of scattering from three-dimensional complex targets. In: Computational Electromagnetics Workshop; 30–31 August 2007; İzmir, Turkey. pp. 26–30.

[9] Pan XM, Pi WC, Yang ML, Peng Z, Sheng XQ. Solving problems with over one billion unknowns by the MLFMA. IEEE T Antenn Propag 2012; 60: 2571–2574.

[10] Deschamps GA. Ray techniques in electromagnetic. P IEEE 1972; 60: 1022–1035.

[11] Lee SW, Sheshadri MS, Jamnejad V, Mittra R. Reflection at a curved dielectric interface: geometrical optics solution. IEEE T Microw Theory 1982; 30: 12–19.

[12] Balanis CA. Advanced Engineering Electromagnetics. 2nd ed. New York, NY, USA: Wiley, 2012.

[13] Tzoulis A, Eibert TF. A hybrid FEBI-MLFMM-UTD method for numerical solutions of electromagnetic problems including arbitrarily shaped and electrically large objects. IEEE T Antenn Propag 2005; 53: 3358–3366.

[14] Ling H, Chou RC, Lee SW. Shooting and bouncing rays: calculating the RCS of an arbitrarily shaped cavity, IEEE T Antenn Propag 1989; 37: 194–205.

[15] Ling H, Lee SW, Chou RC. High frequency RCS of open cavities with rectangular and circular cross sections. IEEE T Antenn Propag 1989; 37: 648–654.

[16] Jin JM, Ling F, Carolan ST, Song JM, Gibson WC, Chew WC, Lu CC, Kipp R. A hybrid SBR/MoM technique for analysis of scattering from small protrusions on a large conducting body. IEEE T Antenn Propag 1998; 49: 1349–1357.

[17] Tao Y, Lin H, Bao H. GPU-based shooting and bouncing ray method for fast RCS prediction. IEEE T Antenn Propag 2010; 58: 494–502.

[18] Chen SH, Jeng SK. An SBR-image approach for radio wave propagation in indoor environments with metallic furniture. IEEE T Antenn Propag 1997; 45: 98–106.

[19] Weinmann F. Ray tracing with PO/PTD for RCS modeling of large complex objects. IEEE T Antenn Propag 2006; 54: 1797–1806.

[20] Hazlett M, Andersh DJ, Lee SW, Ling H, Yu CL. XPATCH: a high-frequency electromagnetic scattering prediction simulator using shooting and bouncing rays. Proceedings of SPIE 1995; 2469: 266–275.

[21] ShipEDF. Simulation Environment for the EM Design of Modern Ship. Pisa, Italy: IDS Ingegneria dei Sistemi S.P.A.

[22] Zhang R, Hong J, Ming F. CASpatch: A SAR image simulation simulator to support ATR applications. In: 2nd Asian-Pacific Conference on SAR; 26–30 October 2009, Xian, Shanxi. pp. 502–505.

[23] Weinmann F, Nitschkowski J. A SBR simulator with GO-PO for calculating scattered fields from coated surfaces. In: Proceedings of the 4th European Conference on Antennas and Propagation; 12–16 April 2010, Barcelona, Spain. pp. 1–4.

[24] FEKO Suite 6.0. EM Software and Systems. Available at http://www.feko.info. 2010.

[25] Asvestas JS. The physical optics method in electromagnetic scattering. J Math Phys 1980; 21: 290–299.

[26] Zhenghong G, Mingliang W. An efficient algorithm for calculating aircraft RCS based on the geometrical characteristics. Chinese Journal of Aeronautics 2008; 21: 296–303.

[27] Fernandez-Recio R, Jurado-Lucena A, Errasti-Alcala B, Poyatos-Martinez D, Escot- Bocanegra D, Montiel-Sanchez I. RCS measurements and predictions of different targets for radar benchmark purpose. In: International Conference on Electromagnetics in Advanced Applications; 14–18 September 2009, Torino, Italy. pp. 443–446.

[28] Griesser T, Balanis C. Backscatter analysis of dihedral corner reflectors using physical optics and the physical theory of diffraction. IEEE T Antenn Propag 1987; 35: 1137–1147.

[29] Gallman P. Radar Reflectors for Cruising Sailboats: Why They Work, What the Limitations Are and How to Evaluate Them. Los Angeles, CA, USA: Ulyssian Publications, 2005.

[30] Woo AC, Wang HTG, Schuh MJ, Sanders ML. EM programmer's notebook-benchmark radar targets for the validation of computational electromagnetics programs. IEEE Antennas Propag 1993; 35: 84–89.

[31] Griesser T, Balanis CA, Liu K. RCS analysis and reduction for lossy dihedral corner reflectors. P IEEE 1989; 77: 806–814.

[32] Özdemir C. Synthetic aperture radar. In: Chang K, editor. The Wiley Encyclopedia of RF and Microwave Engineering. New York, NY, USA: Wiley-Interscience, 2005. pp. 5067–5080.

[33] Yılmaz B. Calculation of electromagnetic scattering from large and complex targets and obtaining their inverse synthetic aperture radar images. MSc, Mersin University, Mersin, Turkey, 2008.